ORIGINAL PAPER

Nonlinear interferometric vibrational imaging for fast label-free visualization of molecular domains in skin

Wladimir A. Benalcazar · Stephen A. Boppart

Abstract The most prevalent molecular constituents of skin are spatially mapped by the use of nonlinear interferometric vibrational imaging, a coherent anti-Stokes Raman scattering (CARS)-based technique. Raman-like profiles over the range from 2,800 to 3,000 cm^{-1} are acquired by means of completely suppressing the non-resonant background, allowing the generation of images based on the molecule-specific spectral profiles over the probed region with high spatial resolution. A simple algorithm that maps spectral content to color allows the visualization of histology in a manner analogous to that obtained with more conventional staining procedures (e.g., hematoxylin-eosin), but faster and with the benefit of having access to localized spectra, which could further enhance the potential for diagnosis of diseases, especially during the early stages of development.

W. A. Benalcazar · S. A. Boppart (✉)
Department of Electrical and Computer Engineering,
Biophotonics Imaging Laboratory,
Beckman Institute for Advanced Science and Technology,
University of Illinois at Urbana-Champaign,
Urbana, IL 61801, USA
e-mail: boppart@illinois.edu

S. A. Boppart
Department of Bioengineering, Biophotonics Imaging Laboratory,
Beckman Institute for Advanced Science and Technology,
University of Illinois at Urbana-Champaign,
Urbana, IL 61801, USA

S. A. Boppart
Department of Medicine, Biophotonics Imaging Laboratory,
Beckman Institute for Advanced Science and Technology,
University of Illinois at Urbana-Champaign,
Urbana, IL 61801, USA

Introduction

In pathology, the histological examination of tissues is the gold standard for the diagnosis of a number of diseases, including cancer. The investigation of the micro-structural organization of tissue requires proper differentiation of the cellular types, as well as extracellular components. The conventional method to achieve this involves processing resected tissue from the patient's body through a series of chemical reactions that eventually stain the tissue based on its molecular composition, so that the different cellular and extracellular components can be differentiated under a bright-field microscope. This method, however, is both invasive and time consuming, and has therefore motivated the investigation of alternative imaging approaches, such as those based on the excitation of nonlinear optical processes in the sample to provide molecular contrast in a non-invasive fashion.

The present work makes use of nonlinear interferometric vibrational imaging (NIVI) [1] to optically interrogate the molecular content of ex vivo porcine skin over a vibrational range from 2,800 to 3,000 cm^{-1}. This range is shown to provide sufficient selectivity to discriminate the main constituents of skin without the introduction of exogenous markers or labels, as in the more conventional histopathological staining techniques. The contrast in NIVI resides in the third-order nonlinear optical susceptibility of the sample, by which molecular vibrational modes are excited in a nonlinear scattering process that uses a triplet of optical pulses: the pump, the Stokes, and the

probe, in a process known as coherent anti-Stokes Raman scattering (CARS) [2] (Fig. 1).

Spontaneous Raman scattering, another optical spectroscopic technique that interrogates the third-order susceptibility of samples, has shown intrinsic chemically specific contrast for a wide variety of biologically relevant constituents [3] and has been used in the identification of a number of diseases [4–6]. However, fast imaging is precluded for this technique due to the long integration times needed for signal acquisition with sufficiently high signal-to-noise ratio, thus limiting its applications in both the biological and medical fields. This problem is overcome in CARS-based approaches, where the number of scattered photons, the so-called anti-Stokes photons, is orders of magnitude higher than in spontaneous Raman microscopy [7].

Additionally, anti-Stokes photons are blue-shifted with respect to the incident pulses, facilitating their spectral separation from the excitation, and are generated exclusively at the focus, providing intrinsic three-dimensional optical sectioning ability. CARS also exhibits advantages over infrared (IR) spectroscopy, which measures the direct absorption of IR photons that excite vibrational modes in molecules. In particular, the low excitation wavelengths used in IR spectroscopy lower its resolution and the high levels of absorption of IR photons by water hinders its application to image living cells.

CARS microscopy has been demonstrated as an effective imaging method for biological specimens by exploiting the strong response in the CH stretching region of the spectrum from 2,800 to 3,100 cm^{-1}. It has subsequently found
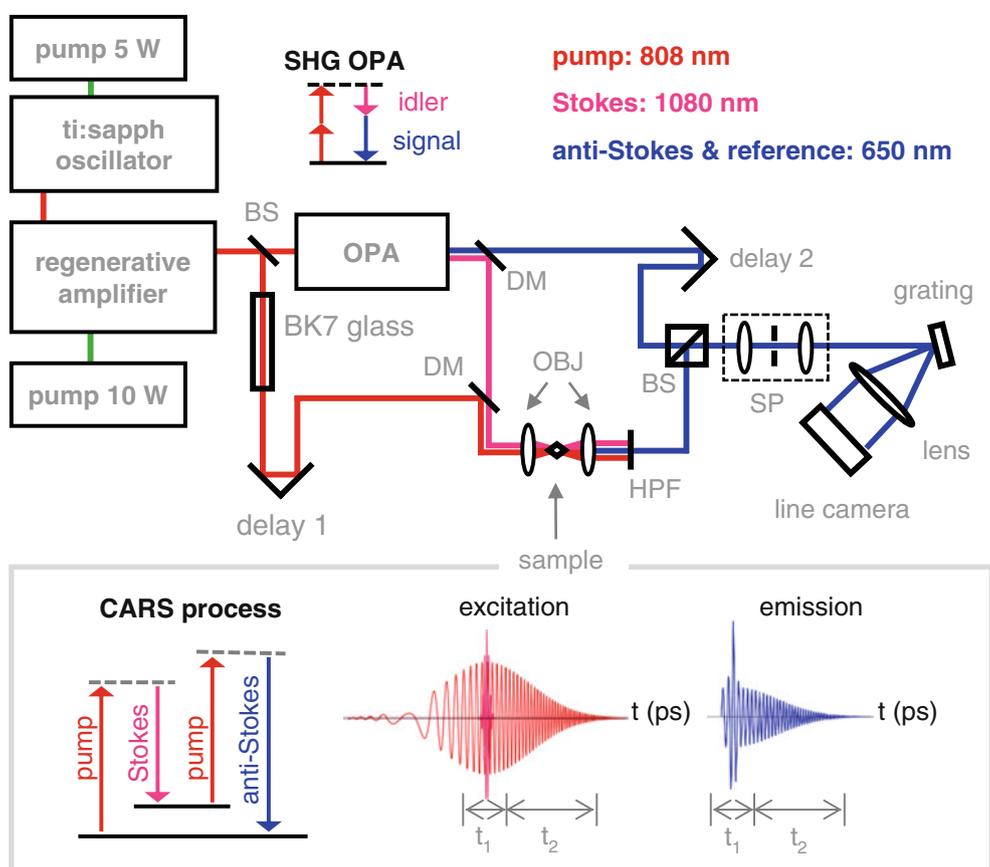

Fig. 1 Nonlinear interferometric vibrational imaging experimental set up. For this study, 100 fs pulses at 808 nm from a titanium/sapphire oscillator are amplified by a regenerative amplifier to 4 μJ of energy at 250 kHz. A portion (10%) of the power is used as the pump and the pulses are chirped by passing them through 85 cm of BK7 glass, expanding them to a duration of 6 ps. The remaining power is used in a second harmonic generation optical parametric amplifier to generate a signal at 650 nm and an idler at 1,050 nm. The latter serves as the Stokes pulses. The pump and Stokes pulses are overlapped spatially and temporally (delay 1) at the sample. The generated coherent anti-Stokes Raman scattering (CARS) signal is chirped, following the chirp of the pump, which also acts as a probe. During the overlap of pump and Stokes (t_1), there are both resonant and non-resonant contributions. As soon as the Stokes vanishes, only resonant CARS persists, until it reaches its dephasing time (t_2). To reconstruct the vibrational response of the molecule, the CARS pulses are resolved in time by mixing them with the transform-limited signal from the SHG-OPA and diffracting the combined pulses into a CCD camera. A telescope with a 20 μm diameter pinhole is used to spatially filter the reference signal and reject elastically scattered CARS photons. A second delay (delay 2) is used to ensure the reference pulses cause interference patterns within the resolution limits of the camera. Abbreviations: *BS* beam splitter, *DM* dichroic mirror, *HPF* high pass filter, *OBJ* objective lenses, *SP* spatial filter

applications in imaging lipid-rich structures [8], and has shown sufficient sensitivity to spatially map lipid-droplet organelles [9] and lipid bilayers [10]. As suggested by spontaneous Raman spectroscopy, extending the vibrational range targeted by CARS to the fingerprint region would enable selectivity over the backbone of proteins and nucleic acids, or even specific amino acids and nucleotides [11, 12]. However, the presence of a non-resonant background (NRB) that coherently mixes with the resonant signal from the weak bands in this region of the spectrum overwhelms and significantly distorts the signatures. In biological systems, the NRB mainly arises from water. Suppressing it represents a major challenge, even in the recovery of spectra in the CH stretching region, where resonant signals are much stronger.

In our NIVI approach, the NRB is minimized by optically driving the vibrations of the molecules during their entire coherence time. This is done in the absence of the Stokes field, which is used exclusively during the initial excitation of the vibrational states (Fig. 1). This is advantageous because, while the coherence time in molecules is of the order of picoseconds, the NRB responds instantaneously [13]. Therefore, most of the optical power of the probe pulse is used in the generation of resonant signal following the excitation. This scheme constitutes an advanced version of time-resolved CARS, which delays the probe pulse with respect to the pump and Stokes pulses [14, 15], because NIVI reduces the number of excitation pulses from three to two and generates resonant anti-Stokes photons during the entire time of vibration of the molecule (i.e., at a continuum of delays), as opposed to at a single delay. However, the associated increase in resonant signal compared to rime-resolved CARS expense of generating a remnant NRB during the initial excitation of the vibrations. This remnant NRB is further eliminated using a phase-sensitive interferometric detection scheme that enables the reconstruction of the complete complex spectrum of the anti-Stokes signal, from which its imaginary component can be separated. The advantage of obtaining this imaginary component is not only the possibility of achieving full suppression of NRB, but also to increase the spectral resolution, because the real part of the resonant response, which adds width to the spectral lines, is also suppressed. This has led to the retrieval of spectra that resemble those of Raman spectroscopy in both pure lipid samples [16] and tissues [17, 18].

Recently, the maximum entropy (ME) algorithm [19] has been successfully adopted by groups that seek suppression of NRB by means of identifying the imaginary component of the complex anti-Stokes field. However, contrary to our hardware-based approach, the ME algorithm may add processing time to the imaging sessions. A more recent algorithm [20] based on the same principle used in the retrieval of spectra in NIVI [21] has been presented, which

does not require interferometric detection. The above mentioned methods could be advantageous from the point of view of implementation, as interferometry complicates the experimental set-up. On the other hand, interferometry has as an advantage the linear dependence of the signal on the analyte, and the amplification associated with the mixing of the signal with a reference, resulting in shot-noise-limited detection.

Besides time-resolved CARS, hardware-based alternative approaches for the suppression of NRB include polarization CARS, which blocks the NRB by taking advantage of the fact that the NRB is generated with a different polarization than the resonant signal [22], and pulse-shaping approaches to CARS, which aim to cause destructive interference of the NRB by shaping the phase of the incident pulses [23]. However, such methods usually come at the expense of also reducing or altering the resonant signal of interest.

In this work, we optically interrogate the molecular composition of ex vivo porcine skin, a good representative model for human skin [24], to show how suppression of the background over a broadband vibrational range can expand the selectivity of CARS. In the past, FT-IR [25] and Raman [26, 27] spectroscopy have characterized the spectral profiles for the main constituents of skin, and current label-free imaging of skin that discriminates elastin, collagen, and lipids has been performed by multimodal techniques using CARS, multiphoton excited auto-fluorescence, and second harmonic generation (SHG) [28–30]. Furthermore, real-time CARS imaging in vivo has been demonstrated in skin [31] but without broadband microspectroscopic content. Here, we demonstrate that the retrieval of broadband spectra over the CH stretching region is sufficient to discriminate the stratum corneum, epidermis, and dermal stroma, as well as collagen and adipose domains in the subcutaneous tissue, provided that the NRB is fully suppressed.

Methods

A schematic of the imaging system used in this study is shown in Fig. 1. This NIVI system differs from conventional CARS systems in that both the pump and the Stokes are femtosecond pulses, as opposed to picosecond pulses. Furthermore, these pulses, as well as a third pulse to serve as reference, need to be phase locked. The wide bandwidth of the Stokes pulses (25 nm bandwidth centered at 650 nm) allows for spanning the range of vibrations from 2,790 to 2,970 cm^{-1} (FWHM), such as in conventional broadband CARS systems [32]. The three pulses used in this set-up (two for CARS generation and a third one for interferometry) are derived from pulses of 25 nm in bandwidth, centered at 808 nm at an 80 MHz repetition rate from a titanium:sapphire oscillator (Mira, Coherent Inc., Santa Clara, CA), which are

amplified by a regenerative amplifier (RegA 9000, Coherent Inc., Santa Clara, CA) to provide pulses of 4 μJ at 250 kHz. A beam splitter separates a fraction of this power to be used as the pump-probe beam. This pump pulse is chirped for the purpose of minimizing the NRB while maximizing the extraction of the resonant response of the molecule, i.e., it is temporally expanded beyond the duration of the response of the NRB to drive the vibrations of the sample during its entire coherence time. The remaining power is directed to a second harmonic optical parametric amplifier (OPA 9450, Coherent Inc. Santa Clara, CA), from which the idler is used as Stokes pulses, and the signal is used as reference pulses. Besides locking the phases of the resulting beams, this method ensures, via conservation of energy in the SHG-OPA process at the OPA crystal, that the reference pulses will always be in the same bandwidth as the CARS signals, which is convenient when tuning the OPA for targeting different parts of the vibrational spectrum. Since the signal and idler from the OPA are generated through non-resonant transitions in the second harmonic crystal, they preserve the phase of the incident pulses, which are close to transform limited (a compressor prior to the OPA, not shown in the schematic of Fig. 1, is used to compensate phase dispersion). What remains is a small phase profile that is further corrected during data processing.

At the sample, the transform limited Stokes and the chirped pump pulses generate an anti-Stokes signal that is initially both resonant and non-resonant. The non-resonant signal quickly decays as the Stokes pulse ends, and only a purely resonant anti-Stokes signal follows as the result of the chirped pump driving the vibrations of the molecules until they reach their dephasing time. The powers at the sample are 10 mW for the pump and 2 mW for the Stokes. CARS signal is generated at a focal volume characterized by a lateral resolution of 1.4 μm and a Rayleigh range of 11 μm. Finally, these CARS pulses are reconstructed in time by the use of spectral interferometry, from which the real and imaginary components of their spectra are discriminated.

NIVI imaging was performed by scanning the sample across the focused beam and collecting the forward directed anti-Stokes pulses. At each pixel, the CARS signal and the delayed reference pulses are mixed and diffracted on to a CCD camera. In order to reject photons that have undergone multiple elastic scattering events in the sample, as well as to smooth the profile of the reference pulses, the mixed signal is passed through a spatial filter, placed just before the diffraction grating. The integration time is 10 μs/pixel for skin, however, our current scanning mechanism is slow, and an image of 200×200 pixels requires about 6 min. The three-dimensional (two spatial and one spectral) datasets were post-processed following a sequence of steps detailed in our previous work [16, 17,

21]. Briefly, the procedure consists on retrieving the cross-interferometric term from the interference pattern at the camera, taking its inverse Fourier transform, setting its delay with respect to the reference to zero and compensating the phase for the chirp induced by the pump pulses in the time domain, taking its Fourier transform, and separating the real and imaginary components of the resultant complex spectrum, which contain the NRB and the NRB-free Raman-like spectral lines, respectively.

Skin imaging

In this study, sets of two adjacent tissue sections were cryosectioned: one unstained section for NIVI imaging (50 μm thick), and one stained with standard hematoxylin and eosin (H&E) to serve as a reference. The procedure for image construction is shown in Fig. 2 for a sample of subcutaneous tissue. As in conventional CARS, intense signal are indicative of lipids [8]. However, such approach is not a sufficient indicator of lipid content. The intensity of the signal can vary due to concentration differences within the sample, or due to elastic scattering processes when anti-Stokes pulses generated at the focus encounter dense structures out-of-focus in thick tissues (see Fig. 2a). For the purpose of labeling the images chemically, the retrieved spectrum at each pixel s_Ω was simplified by dividing it into the five spectral bands encountered for biological macromolecules in this spectral region, as obtained by various Raman-based studies of skin [26, 33]. The five bands have boundaries Ω_i. $i=1$ to 6, as listed in Table 1. To each band, a value b_j, $j=1$ to 5 was assigned as the average spectrum within its limits. To avoid the effect of the power of the signal in the classification, the simplified spectra were normalized to have unit area. This corresponds to a reduction of the spectral content by means of the calculation:

$$b_j = \frac{\sum_{\Omega_j}^{\Omega_{j+1}} s_\Omega}{A} \tag{1}$$

with $A = \sum_{\Omega_1}^{\Omega_6} s_\Omega$ and for $j=1$ to 5. Following this, contrast emerged at three of the five spectral bands, which indicates the presence of different species, because the values of the spectral bands, after normalization with respect to the spectrum area, correspond to taking ratios that are shape dependent. For each band, a corresponding image indicates the relative contribution of that specific vibration to the entire vibrational spectrum.

Contrast in these images arises when targeting two clearly defined spectroscopic domains: the first one corresponds to regions rich in lipids, with high vibrational bands at 2,845, 2,880, and 2,930 cm^{-1}, and the second one

Fig. 2 Algorithm used in the construction of molecular images with nonlinear interferometric vibrational imaging (NIVI). (**a**) Image showing the intensity of the CARS resonant signal by integrating the entire vibrational spectrum at each pixel. (**b**) Methyl oleate and collagen spectra as obtained by spontaneous Raman spectroscopy showing the vibrational bands existing in the targeted region (the rightmost vibration at 3,015 cm^{-1} was marginally covered by NIVI). The *colors* indicate the corresponding color channels assigned to bands 1, 4, and 5 in the formation of the composite image that provides chemical contrast. (**c–e**) Images at each channel and (**f–h**) corresponding histograms. The dynamic range of each channel is maximized before merging them into the composite. (**i**) Composite NIVI image showing differentiation of lipids (*red*) and stroma (*green-blue*) in subcutaneous tissue. (**j**) Corresponding H&E histology of an adjacent section. The *scale bar* is 100 μm in every image
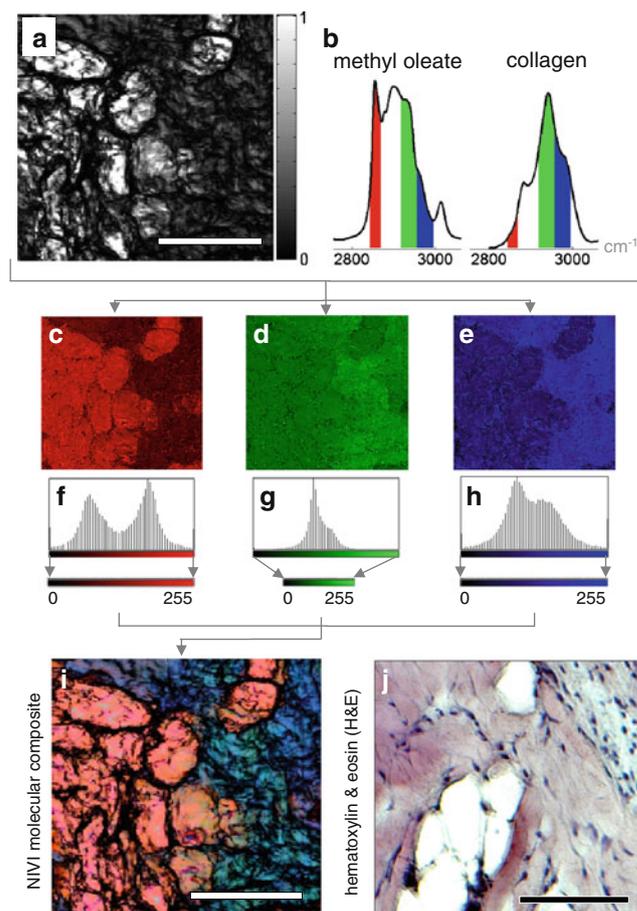
corresponds to stromal regions, rich in collagen and elastin, both of which show a predominant resonance at 2,930 cm^{-1} [34, 35]. Besides these two main domains, keratinized regions, such as the stratum corneum or hair follicles, also showed a distinctive spectral profile. In the images, contrast occurs primarily at bands 1 and 5, and to a lesser extent at band 4, where both domains present high signals (Fig. 2b illustrates this by highlighting bands 1, 4, and 5 with red, green and blue colors, respectively, in two spectra obtained by Raman spectroscopy on pure methyl oleate, a good model for lipids, and collagen type 1 from rat tail tendon). Images at bands 2 and 3 showed no appreciable contrast. The images at bands 1, 4, and 5 were used as the channels of an RGB image that compiles the chemical information (Fig. 2c–h). To avoid noisy regions in the images due to low signal-to-noise ratio (SNR), the RGB composite pixels were de-normalized (by multiplying them by their respective values of A in Eq. 1), thereby restoring the initial intensity in the image. Notice the difference in the composite image in Fig. 2i, where a clear boundary of the lipid and stroma domains is defined, as opposed to the features in Fig. 2a, which lack any specific chemical information other than the high intensity from which the presence of lipids can only be inferred. As a

reference, Fig. 2j shows a bright-field image of an H&E section, the gold standard technique for diagnosis, taken from the same region, which shows correspondence in comparison with the NIVI image.

The method described above was used to map the molecular composition in the outer-most layers of porcine skin from the back region of the animal. While the method devised here starts from a priori knowledge about the bonds to which Raman-based techniques are sensitive in this region, the number of molecular distinctions attainable by the technique cannot be inferred directly prior to the experiment. In this sense, the method is suitable for the interrogation of potentially unknown compositions in skin or other tissues or cells in a fast way. In other methods, such as cluster analysis, the complexity of the classification increases significantly with the number of data points and class numbers, making its employment time consuming. In principal component analysis, another method widely adopted [36, 37], the problem resides in that the classification is difficult to interpret, as the principal components are, in general, expressed in bases other than the range of vibrational frequencies. Therefore, the proposed method presents the advantages of being fast and easy to read,

Table 1 Bands used in the decomposition of spectra for molecular image construction [26, 33]

j	$\Omega_j - \Omega_{j+1}$ (cm^{-1})	Vibration	Contrast?
1	2,842–2,865	CH$_2$ symmetric	Yes
2	2,865–2,890	CH$_2$ anti-symmetric	No
3	2,890–2,913	CH$_3$ symmetric	No
4	2,913–2,955	CH$_3$ symmetric	Yes
5	2,955–3,000	CH$_3$ asymmetric	Yes

which is advantageous in exploratory imaging over large regions, while the alternative above mentioned methods are more suitable for the study and classification of detailed differences over reduced datasets.

Imaging with the proposed method revealed that NIVI is sensitive to four different domains: stratum corneum, hair follicles, dermis, and epidermis. Such differentiation is show in Fig. 3. The resonant signal over the entire probed bandwidth is shown in Fig. 3a, and the NIVI composite image, which features the molecular regions, is shown in Fig. 3b. The corresponding spectra (Fig. 3c), which are in concordance with previous characterization with spontaneous Raman spectroscopy [35], show that the spectral features are similar in pairs: dermis and epidermis show higher concentration of CH$_3$ symmetric resonances, while stratum corneum and follicles show comparable amplitudes at CH$_2$ and CH$_3$ symmetric vibrations. This increase in signal at the CH$_2$ symmetric band when compared to dermis and epidermis captures the presence of lipids in the stratum corneum and sebaceous secretions in the follicles. Modulation of the molecular map by the intensity map gives the composite image of the sample (Fig. 3d), which overlays molecular information with structural features of the tissue, such as the flattened keratinized layers of the stratum corneum, the membranes and nuclei of the dermal cells, and the extracellular collagenous fibers in the dermis. For comparison, an H&E stained section is shown in Fig. 3e, which features the same information as the NIVI composite, but requires long hours of processing, and does not possess the additional spectroscopic content available to NIVI, which would be advantageous as a future diagnostic technique based on quantitative measures of histologic or cytologic composition.

Additionally, subcutaneous tissue was also investigated. Figure 4 shows an image of subcutaneous tissue with a hair follicle. By looking at the intensity image, only high signal from lipids in the adipocytes can be inferred, and the gland structures and stroma become apparent only after reconstruction of the composite (Fig. 4a), in agreement with histology (Fig. 4b) taken from an adjacent tissue section. The color-coding is consistent with those obtained in Fig. 2 (also obtained from subcutaneous tissue), with the difference of having a shift in the color of the stromal regions towards green, indicative of a higher ratio of asymmetric/symmetric CH$_3$ vibrations, which may correspond to different conformation densities or compositions in the stroma (e.g., different proportions of collagen types and/or elastin). In general, a higher concentration of collagen was observed in the subcutaneous stroma compared with stroma in the cutaneous region, as shown in the spectrum obtained from subcutaneous stroma in Fig. 4c, which resembles more that of collagen (Fig. 2b) than the spectra from the dermis and epidermis in Fig. 3c. In general, adipose and stroma domains gave well-defined spectra, (both of which resemble the spectra in Fig. 2b).

Discussion

Although NIVI spectra consist of pure resonant responses, slight differences are evident when compared with spontaneous Raman spectroscopy. In particular, NIVI spectra are weighted by the shape of both the Stokes and the reference bandwidths, which precluded, for example, the use of the band from 3,000 to 3,050 cm^{-1} as a discriminator, since this band lies too far from the excitation and detection spectra. Furthermore, interferometry makes the detection sensitive to polarization. Despite this, NIVI can build its own classification since it shows enough resolution and suppression of background to account for the detailed structure of vibrational spectra in the CH region. Since each color in the composite represents a vibration relevant for the differentiation of tissue species, this scheme allows a straightforward spatial identification of the prevalent molecular constituents of skin, which does not rely on the excitation of distinctive resonances associated to them, but rather on their unique spectral profiles in the CH stretching region; for example, red pixels map to species with high proportion of signal coming from the band at ~2,845 cm^{-1} relative to the entire profile, while blue pixels are indicative of the band at ~2,956 cm^{-1}. An example of such differentiation exists between the dermis, epidermis, and stroma from subcutaneous tissue, to which small differences in spectra correspond to different tones about the same base color. The differentiation also occurs with lipids from adipocytes and sebaceous glands, as found in the subcutaneous tissue (spectra shown in Fig. 4d), which likely originate from different types of fatty acid chains. Colors in between these most basic ones can be interpreted as mixtures of different species. The interpretation of variations in spectra as originating proportionally from mixtures of different species has basis in the fact that no intermolecular interactions occur that would modify the bands [33], and that the interferometric detection results in signals that are linearly proportional to the susceptibility of the sample, not quadratically proportional, as in conventional non-interferometric CARS techniques.

Fig. 3 Molecular imaging of cutaneous tissue. (**a**) Intensity image (total integrated spectral power). (**b**) NIVI composite showing discrimination of stratum corneum (*sc*), epidermis (*epi*), dermis (*der*), and hair follicle (*fol*). (**c**) NIVI spectra for each domain in (**b**), as obtained by cluster analysis: each spectrum is the result of averaging the spectra of the members of most prevalent cluster in regions of 20×20 pixels^2 within each domain. (**d**) NIVI image showing both structural and molecular compositions. (**e**) H&E histology of a section from the same region. The *scale bar* is 100 μm in every image


scale bars = 100μm
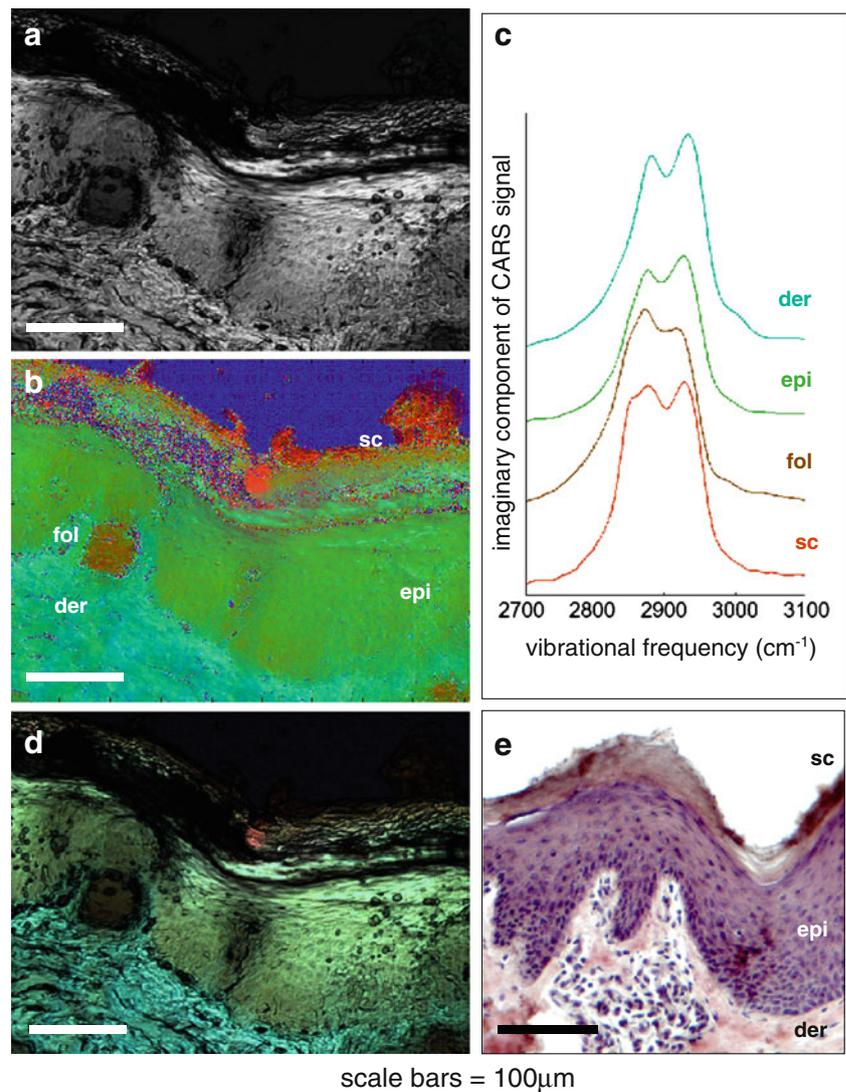
Interferometric detection requires a well-defined phase relationship between the optical fields. As samples get thicker, elastic scattering, and to a lesser extent dispersion, will affect this relationship. To overcome scattering, a pinhole confocal with respect to the focus at the sample was used to block photons that deviate from its original course, a method that has been effective even for samples as thick as 50 μm, as shown in this work. As samples get thicker, however, more scattering events will cause more rejection of light, to a point where the SNR significantly deteriorates. The feasibility of conserving the phase relationship when collecting reflected CARS light still remains to be determined, and is critical to enable in vivo clinical applications. Studies have shown that CARS scattered in the backward direction occurs for small scatterers, and is hindered as they increase in size [38]. Although backward (epi) CARS can originate from backward reflected CARS that initially was emitted in the forward direction, these photons will not be of use for NIVI,

as they most likely will acquire significant phase changes. Regarding penetration depth, other studies in skin tissue have shown that CARS images can be generated as deep as 125 μm, limited by the working distance of the objective, and which is comparable with imaging penetration depths attained by two-photon excited fluorescence using the same objective [31]. Since near-infrared excitation was used, the available power in our set-up was sufficient to effectively excite the sample without damaging the tissue. However, the high intensity of signals originating from lipids, compared with the low signals of other compounds such as keratin, caused the dynamic range in the detection system to be marginal, thus causing, for example, the difficulty in simultaneously obtain high signals for dermis and stratum corneum in Fig. 3 or distinguishing the signal from the hair bulb and shaft in Fig. 4.

Fast microspectroscopic imaging of skin can enable a variety of studies as it could facilitate the visualization and

Fig. 4 Molecular imaging in subcutaneous tissue. (**a**) NIVI composite of hair follicle denoting red signal for lipids and green signal for stroma. (**b**) Corresponding H&E histology from an adjacent section. (**c**) NIVI spectra from adipose and stroma regions extracted from pixels in (**a**), which resemble the spectra from methyl oleate and collagen, shown in Fig. 2b, since these represent good models for the constituents of the adipose and stroma regions. Differences between NIVI and Raman spectra are attributed to bandwidth limitations and polarization sensitivity (see text). (**d**) Spectral differences between lipids in subcutaneous tissue. The *scale bar* is 200 μm in every image
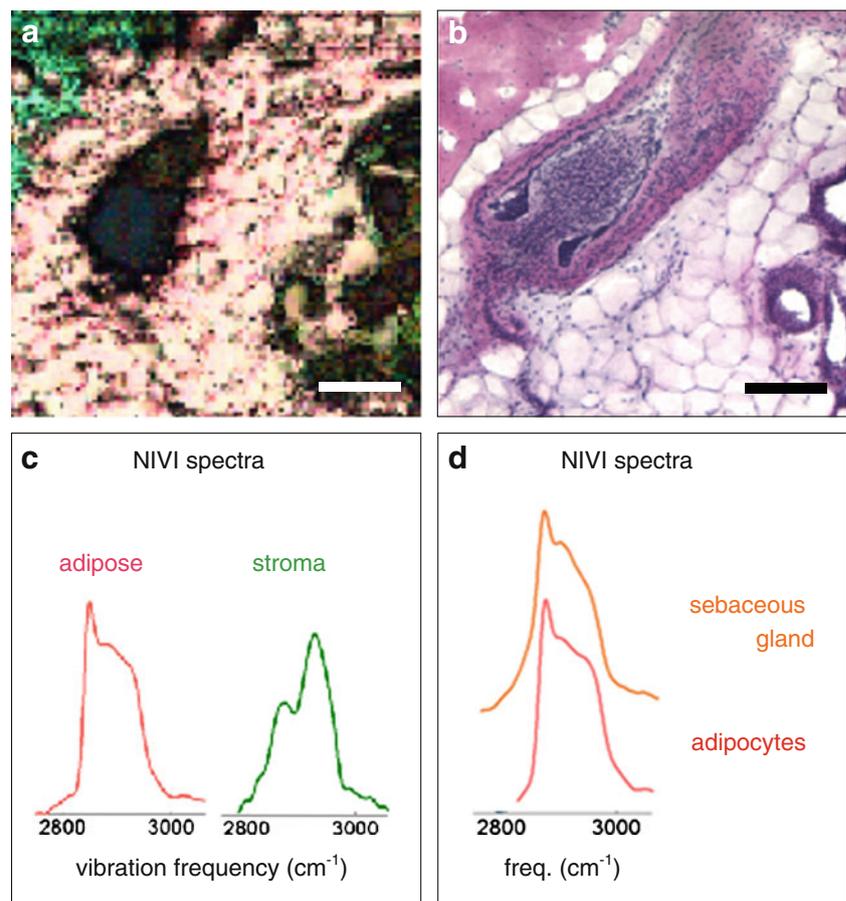
elucidation of important chemical pathways [39] with sufficient spatial and temporal resolution, and with the benefit of having a quantitative assessment of molecular content. Currently, lipids from sebaceous glands and adipocytes in subcutaneous tissue can be discriminated with NIVI based on the intensities at bands 2,845 and 2,956 cm^{-1} [30] (Fig. 4d).

Further improvement of the spatial resolution of our system could allow the differentiation of various kinds of lipids in the stratum corneum, namely, ceramides, cholesterol, and fatty acids present in the complex lipid matrix in which cornecytes are embedded [33]. All three of these compounds have unique and distinctive spectral profiles in the CH region [26, 34]. Since lipids in the stratum corneum provide the primary transport resistance in the skin [25], investigations in this area would help clarify the role of the different lipids in creating this barrier property, which could have implications in the treatment of skin disease and transdermal drug delivery [40].

Due to the fact that signals from collagen and keratin are weaker than for lipids, current imaging of collagen is dominated by the use of second harmonic generation

microscopy, often in multimodal approaches, which has provided a means for the identification of precancerous anomalies [28, 29]. Furthermore, multimodal microscopy has also been used to establish relationships between signal levels and skin age [30, 41]. In general, nonlinear microscopy techniques have great potential for diagnostic purposes. Fluorescence microscopy has shown significant advances in imaging tissue [42]. However, more information is needed to characterize the fluorescence of skin tumors by comparing them with traditional histopathology results before non-invasive fluorescence-based biopsies can become a reality [42]. Fast microspectroscopic vibrational imaging can further improve the selectivity by adding spectral information to the images, an advantage that would greatly benefit by targeting the fingerprint region (e.g., contrast in types of keratins can be obtained by differentiating the relative content of glycine over cystein [35]). Contrary to multimodal techniques, NIVI has the benefit of adding quantitative information about the relative proportions of species. This is not readily obtained with multimodal techniques, as each contrast mechanism has its own scattering cross-section efficiency.

Thus, NIVI has potential for a more quantitative assessment of the internal chemistry of processes in tissues, with applications in both science and medicine.

Conclusions

Nonlinear interferometric vibrational imaging, which uses two femtosecond near-infrared optical pulses to excite and drive vibrations in molecules, has shown successful differentiation of the main molecular domains in ex vivo skin. Accompanying the efficient extraction of vibrational signatures, a systematic and straightforward method for representing and displaying the information in an intuitive manner was presented. This showed that, beyond the differentiation of the main constituents in tissues (e.g., keratin in stratum corneum, collagen in stroma, and lipids in adipocytes), more subtle variations can be made evident.

Key to our experimental set-up was the use of an interferometric detection scheme, which constitutes an efficient method to suppress the NRB, enables shot-noise-limited detection, and allows for the chirped emission of anti-Stokes pulses. All these conditions are important factors that are needed to target other interesting vibrational regions, such as the fingerprint region, which will open many new applications for this technique and imaging method.

References

1. Marks DL, Boppart SA (2004) Phys Rev Lett 92:123905
2. Cheng JX, Xie XS (2004) J Phys Chem B 108:827–840
3. Thomas GJ (1999) Annu Rev Biophys Biomol Struct 28:1–27
4. Huang Z, McWilliams A, Lui H, McLean DI, Lam S, Zeng H (2003) Int J Cancer 107:1047–1052
5. Teh SK, Zheng W, Ho KY, Teh M, Yeoh KG, Huang Z (2008) J Biomed Opt 13:034013
6. Nijssen A, Schu T, Heule F, Caspers P, Hayes D, Neumann M, Puppels G (2002) J Invest Dermatol 119:64–69
7. Petrov GI, Arora R, Yakovlev VV, Wang X, Sokolov AV, Scully MO (2007) Proc Natl Acad Sci USA 104:7776–7779
8. Wang H-W, Fu Y, Hu TB, Le TT, Wang H, Cheng JX (2009) Vib Spectrosc 50:160–167
9. Nan X, Potma EO, Xie XS (2006) Biophys J 91:728–735
10. Potma EO, Xie XS (2003) J Raman Spectrosc 34:642–650
11. Guicheteau J, Argue L, Hyre A, Jacobson M, Christesen SD (2006) SPIE 6218:62180
12. Fodor SPA, Rava RP, Hays TR, Spiro TG (1985) J Am Chem Soc 107(6):1520–1529
13. Marks DL, Vinegoni C, Brefeldt JS, Boppart SA (2004) Appl Phys Lett 85:5787–5789
14. Volkmer A, Book LD, Xie XS (2002) Appl Phys Lett 80:1505–1507
15. Pestov D, Murawski RK, Ariunbold GO, Wang X, Zhi M, Sokolov AV, Sautenkov VA, Rostovtsev YV, Dogariu A, Huang Y, Scully MO (2007) Science 316:265–268
16. Chowdary PD, Benalcazar WA, Jiang Z, Marks DM, Boppart SA, Gruebele M (2010) Anal Chem 82(9):3812–3818
17. Benalcazar WA, Chowdary PD, Jiang Z, Marks DL, Chaney EJ, Gruebele M, Boppart SA (2010) J Select Topics Quant Elect 16(4):824–832
18. Chowdary PD, Jiang Z, Chaney EJ, Benalcazar WA, Marks DL, Gruebele M, Boppart SA (2010) Cancer Res 70(23):1–8
19. Vartiainen EM, Rinia HA, Müller M, Bonn M (2006) Opt Express OSA 14:3622–3630
20. Liu Y, Lee YJ, Cicerone MT (2009) Opt Lett 34:1363–1365
21. Jones GW, Marks DL, Vinegoni C, Boppart SA (2006) Opt Lett 31:1543–1545
22. Cheng JX, Book LD, Xie XS (2001) Opt Lett 26:1341–1343
23. Oron D, Dudovich N, Silberberg Y (2003) Phys Rev Lett 90:213902
24. Jacobi U, Kaiser M, Toll R, Mangelsdorf S, Audring H, Otberg N, Sterry W, Lademann J (2007) Skin Res Technol 13:19–24
25. Ongpipattanakul B, Francoeur ML, Potts RO (1994) Biochimica et Biophysica Acta (BBA)-Biomembranes 1190(1):115–122
26. Wegener M, Neubert R, Rettig W, Wartewig S (1996) Intl J Pharmaceutics 128(1–2):203–213
27. Wegener M, Neubert R, Rettig W, Wartewig S (1997) Chem Phys Lipids 88(1):73–82
28. Lin S-J, Jee S-H, Kuo C-J, Wu R-J, Lin W-C, Chen J-S, Liao Y-H, Hsu C-J, Tsai T-F, Chen Y-F, Dong C-Y (2006) Opt Lett 31(18):2756–2758
29. Skala MC, Squirrell JM, Vrotsos KM, Eickho JC, Gendron-Fitzpatrick A, Eliceiri KW, Ramanujam N (2005) Cancer Res 65(4):1180–1186
30. Koehler MJ, Konig K, Elsner P, Buckle R, Oct Kaatz M (2006) Opt Lett 31(19):2879–2881
31. Evans CL, Potma EO, Puoris'haag M, Ct D, Lin CP, Xie XS (2005) Proc Natl Acad Sci USA 102(46):16807–16812
32. Wurpel GWH, Schins JM, Muller M (2002) Opt Lett 27:1093–1095
33. Percot A, Laeur M (2001) Biophys J 81:2144–2153
34. Slipchenko MN, Le TT, Chen H, Cheng J-X (2009) J Phys Chem B 113(21):7681–7686
35. Williams AC, Edwards HGM, Barry BW (1994) J Raman Spectrosc 25:95–98
36. Lin CY, Suhalim JL, Nien CL, Miljkovic MD, Diem M, Jester JV, Potma EO (2011) J Biomed Optics 16:021104
37. Pohling C, Buckup T, Motzkus M (2011) J Biomed Optics 16:021105
38. Volkmer A, Cheng JX, Xie XS (2001) Phys Rev Lett 87:023901
39. Nicolaides N (1965) J Am Oil Chem Soc 42:708–712
40. Knutson K, Potts R, Guzek D, Golden G, McKie J, Lambert W, Higuchi W (1985) J Control Release 2:67–87
41. Lin S-J, Wu R-J, Tan H-Y, Lo W, Lin W-C, Young T-H, Hsu C-J, Chen J-S, Jee S-H, Dong C-Y (2005) Opt Lett 30(17):2275–2277
42. Palero JA, deBruijn HS, van der Ploeg van denHeuvel A, Sterenborg HJ, Gerritsen HC (2007) Biophys J 93(3):992–1007